



# Corrosion behavior of a spark plasma sintered Fe–20Mn–11Al–1.8C–5Cr alloy in molten aluminum

Jian Liu<sup>1,2</sup> · Wei-ping Chen<sup>1</sup> · Xian-man Zhang<sup>3</sup> · Zhi-qiang Fu<sup>1</sup>

Received: 23 August 2017 / Revised: 23 October 2017 / Accepted: 24 October 2017 / Published online: 28 May 2018  
© China Iron and Steel Research Institute Group 2018

## Abstract

The corrosion behavior of an Fe–20Mn–11Al–1.8C–5Cr alloy prepared by spark plasma sintering was investigated via immersion tests in molten aluminum at 750 °C for 1 and 4 h, respectively, and a hot work steel (AISI H13) was included as a reference. The experimental results show that the corrosion rate of Fe–20Mn–11Al–1.8C–5Cr alloy is ~ 24% of that of H13 steel, suggesting that Fe–20Mn–11Al–1.8C–5Cr alloy in molten aluminum possesses better corrosion resistance than H13 steel. Detailed analysis show that  $\kappa$ -carbide ((Fe, Mn)<sub>3</sub>AlC<sub>x</sub>) and Cr<sub>7</sub>C<sub>3</sub> carbide precipitated in the matrix play a key role in enhancing the corrosion resistance of Fe–20Mn–11Al–1.8C–5Cr alloy in molten aluminum. Both of them show better corrosion resistance than  $\gamma$ -Fe matrix and H13 steel, and can also take on the role of roots in grasping the corrosion product and restrain them from spalling into the molten aluminum.

**Keywords** Fe–Mn–Al–C–Cr alloy · Molten aluminum · Immersion · Corrosion behavior

## 1 Introduction

Corrosion in molten aluminum is usually used to evaluate the durability of material exposed to molten aluminum in many engineering applications such as die casting, containment of liquid aluminum and semisolid processing, since molten aluminum is one of the most aggressive metals to a variety of materials [1]. Corrosion related to Al melt can decrease the service life of working parts directly contacting with molten aluminum and affect the quality of the produced metal or the tolerance of aluminum alloy castings. Most of working parts directly contacting with molten aluminum are made of various steels in the

aluminum industry. Inspection of the literatures [2–5] reveals that molten aluminum can often react with Fe to form two intermetallic layers (Fe<sub>4</sub>Al<sub>13</sub> directly adjacent to the aluminum and Fe<sub>2</sub>Al<sub>5</sub> adjacent to the steel substrate) with hundreds of microns in thickness when pure solid iron/various steels and Al melt come into contact with each other. However, such Fe–Al intermetallics formed in various steels are easy to spalling from the steel and enter into Al melt because of their big thickness, bad compactness and weak bond to the substrate especially when rapid relative motion exists between the steel and molten Al melt, which would facilitate new growth of intermetallics and faster corrosion of substrate. Detachment of these intermetallics and dissolution of Fe into Al melt would lead to the loss of material both at the atomic scale and in blocks. Thus, the corrosion resistance of solid iron and various steels in molten aluminum is usually characterized as unsatisfactory although they have excellent workability, toughness and cheapness. To extend the service life of working parts directly contacting with molten aluminum, new materials, such as Fe–Cr–B cast steel [6] which has high resistance to molten aluminum, are being developed to replace the traditional iron-based alloys.

Despite attempts to develop austenitic Fe–Mn–Al–C alloys with high contents of Mn and Al for corrosion

✉ Wei-ping Chen  
mewpchen@scut.edu.cn

✉ Zhi-qiang Fu  
kopyhit@163.com

<sup>1</sup> Guangdong Key Laboratory for Advanced Metallic Materials Processing, South China University of Technology, Guangzhou 510640, Guangdong, China

<sup>2</sup> College of Engineering and Technology, Normal College of Zunyi, Zunyi 563006, Guizhou, China

<sup>3</sup> Mechanical and Electrical Engineering College, Hainan University, Haikou 570228, Hainan, China

resistance application as a potential substitute for more expensive Fe–Cr–Ni–based stainless steels by replacement of Cr and Ni with less expensive Al and Mn [7], the corrosion resistance of the austenitic Fe–Mn–Al–C alloys was not adequate for applications in many environments. Cr was found to be able to improve the corrosion resistance [8–10] and the high-temperature oxidation resistance [11] of the austenitic Fe–Mn–Al–C alloys. In the study of Fe–Mn–Al–C–Cr alloys, it was found that the Fe–20Mn–11Al–1.8C–5Cr alloy prepared by spark plasma sintering (SPS) consisted of  $\kappa$ -carbide ((Fe, Mn)<sub>3</sub>AlC<sub>x</sub>), Cr<sub>7</sub>C<sub>3</sub> carbide and a trace of Al<sub>2</sub>O<sub>3</sub> which all have good phase stability at elevated temperatures [12] embedded in the  $\gamma$  matrix [13]. Mainly due to the presence of (Fe, Mn)<sub>3</sub>AlC<sub>x</sub> and Cr<sub>7</sub>C<sub>3</sub>, the ultra-fine-grained Fe–20Mn–11Al–1.8C–5Cr alloy processed via spark plasma sintering exhibits good compressive strength at elevated temperatures and high Vickers hardness at room temperature which are higher than those of their as-cast counterparts. However, previous works [14, 15] indicated that the stability of the (Fe, Mn)<sub>3</sub>AlC<sub>x</sub> carbide in Fe–Mn–Al–C alloys was affected by Al content significantly. Thus, the durability of the spark plasma sintered Fe–20Mn–11Al–1.8C–5Cr alloy in pure aluminum melt is of interest. This study systematically investigates the corrosion rate, interfacial morphology and corrosion products of the spark plasma sintering processed Fe–20Mn–11Al–1.8C–5Cr alloy in pure aluminum melt at 750 °C, aiming to provide data for corrosion behavior of this alloy system in molten metal.

## 2 Experimental

### 2.1 Materials tested

In the present study, the Fe–20Mn–11Al–1.8C–5Cr alloy was prepared by using mechanical alloying (MA) with subsequent SPS. MA is a solid-state powder processing technique involving repeated welding, fracturing and rewelding of powder particles. The main advantages of MA are its simple process as well as low cost and ability to prepare supersaturated solid solutions or nanocrystalline structure materials [16]. SPS is a novel process that uses pulsed high DC current with uniaxial pressure to rapidly consolidate powders of metals, ceramics and composite materials [17]. SPS can produce a densely bulk material with a minimal grain growth and a controlled microstructure quickly, which is advantageous to improve the mechanical properties of the bulk [18, 19]. Fe, Mn, Al and Cr (99.9 wt% purity, < 45  $\mu$ m) powders as well as C (99.9 wt% purity, < 600  $\mu$ m) powder were firstly blended with the nominal composition of Fe–20Mn–11Al–1.8C–5Cr (wt%). Then, 100 g of the blend elemental powders and

1000 g of WC grinding balls of 5 mm in diameter were packed in a stainless steel vessel. The milling was carried out in a QM-3SP4 high energy planetary ball mill at 300 r/min, with an ON time of 60 min followed by an OFF time of 10 min. Under an argon atmosphere, the powders were wet milled for 5 h by adding cyclohexane as process control agent (PCA) after 45 h of dry milling. After being dried, the sieved powder of 16 g was subsequently sintered by Dr. Sinter Model SPS-825 Spark Plasma Sintering System at 1100 °C for 5 min at a pressure of 50 MPa under vacuum (residual cell pressure < 8 Pa). The samples were heated to 600 °C within 6 min, while from 600 to 1000 °C and from 1000 to 1100 °C, heating rates were reduced to 50 and 10 °C/min. In addition, the H13 steel widely used in the aluminum industry whose chemical is shown in Table 1 [20] was selected as the contrast material. The measured densities of H13 and Fe–20Mn–11Al–1.8C–5Cr were 7.73 and 6.35 g/cm<sup>3</sup>, respectively. As a typical presentation of microstructures shown in Fig. 1, the tested Fe–20Mn–11Al–1.8C–5Cr alloy consists of  $\gamma$ -matrix,  $\kappa$ -carbide, Cr<sub>7</sub>C<sub>3</sub> carbide and Al<sub>2</sub>O<sub>3</sub>. More details would be found in previous work [13].

### 2.2 Corrosion test

The corrosion tests were conducted in pure Al melt at 750 °C for 1 and 4 h. Before corrosion tests, the test specimens with dimensions of 10 mm  $\times$  7.5 mm  $\times$  7.5 mm were cut from the H13 steels and the as-sintered Fe–20Mn–11Al–1.8C–5Cr samples. All the samples were ground to a 2000-grit finish. After coating five faces of the specimen with ZnO<sub>2</sub>, the specimen was dried, wrapped with graphite paper, held in a graphite die and then dipped into the molten aluminum for 1 h and 4 h. After the corrosion test, all the samples were withdrawn and cooled in air. Based on the chemical equation  $2\text{Al} + 2\text{NaOH} + 2\text{H}_2\text{O} \rightarrow 2\text{NaAlO}_2 + 3\text{H}_2\uparrow$ , soaking the immersed specimens in NaOH solution is one effective method to clean the residual solidified aluminum sticking to samples without effect on iron-based alloy and intermetallics, and 10% NaOH solution has been generally accepted by many researchers and adopted in many applications [21–23]. Thus, the parallel test sample was soaked in a 10 wt% NaOH solution to eliminate the solidified Al sticking to samples before weight losses measurement in this work. Next, the samples were ultrasonically cleaned with acetone and alcohol for thorough sweep of NaOH. Then, volume

**Table 1** Chemical composition of H13 steel (wt%) [20]

Element	C	Si	Cr	Mo	Mn	Ni	V	Fe
Content	0.38	1.0	5.3	1.3	0.4	0.05	0.9	Balance

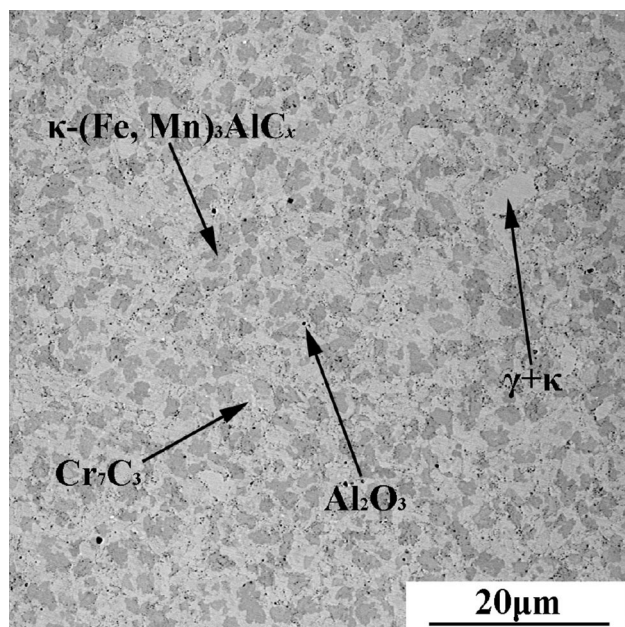


**Fig. 1** SEM image of Fe-20Mn-11Al-1.8C-5Cr alloy consolidated by SPS at 1100 °C for 5 min under pressure of 50 MPa

losses were gained from the measured weight losses. According to Refs. [21, 23], the final corrosion rate ( $V$ ) was expressed in ( $\text{mm}^3 \text{cm}^{-2} \text{h}^{-1}$ ) in present study [21, 23].

The cross-sectional images of the H13 and Fe-20Mn-11Al-1.8C-5Cr samples after being immersed in 750 °C Al melt were investigated in a scanning electron microscope (SEM, Phenom proX, Phenom-World B.V., Netherlands). Element distribution of the corrosion product was analyzed using an electron probe microanalyzer (EPMA-1600). The concentration profiles changes of Fe, Mn, Al, C and Cr from the matrix materials to the outer Al were measured using energy dispersive spectrometer (EDS) line scan. EDS attached to SEM was employed to identify the phase composition of the corrosion products. The phase structure of the reaction products was identified by X-ray diffraction (XRD, D8-Advance, Bruker, Germany).

### 3 Results

#### 3.1 Corrosion resistance

Weight loss per unit time per unit area [22], variation of intermetallic layer thickness with corrosion time [3, 4, 23] and volume loss per unit time per unit area [21, 24, 25] are three typical methods used to characterize corrosion rate of materials in molten metal. The calculation of weight loss directly describes the relative weight change of the test material over the duration of the immersion time. However,

it is unreasonable for the evaluation of materials with different density because of not considering the density difference of various materials. Variation of intermetallic layer thickness with corrosion time is not fit for the corrosion over long time either, because the corrosion products usually break off into molten Al melt as the corrosion time increases. The determination of the volume loss as corrosion rate takes into consideration the breaking off of the formed intermetallics over the given immersion time and the density difference of various materials. The mean corrosion rates of H13 and Fe-20Mn-11Al-1.8C-5Cr alloy in Al melt are shown in Fig. 2. It is obvious that the sintered Fe-20Mn-11Al-1.8C-5Cr alloy exhibits a lower corrosion rate, about 24% of that of H13 steel, suggesting that the corrosion resistance of Fe-20Mn-11Al-1.8C-5Cr alloy in Al melt is better than that of H13 steel.

#### 3.2 Cross-sectional images

Figure 3 shows the cross-sectional images of Fe-20Mn-11Al-1.8C-5Cr and H13 steel after being immersed in 750 °C Al melt for 1 and 4 h, respectively. Figure 3c, d shows that all the corrosion interfaces include substrate, intermetallics and Al for two kinds of test samples. It shows that the corrosion product contains two intermetallics layers, layer L ( $L_1$  and  $L_2$ ) and layer R ( $R_1$  and  $R_2$ ), which lies close to the matrix materials and outer Al, respectively. For both materials, layer L grows into the matrix materials with tongue-like shape, and the thickness of layer L is obviously bigger than that of layer R. As for Fe-20Mn-11Al-1.8C-5Cr alloy, obvious cracks can be observed. It is interesting that the cracks only formed at the interface between layer  $L_2$  and Fe-20Mn-11Al-1.8C-5Cr alloy substrate instead of along with the interface between layer  $L_2$  and layer  $L_2$ , which indicates that the bonding between different layers is stronger. Moreover, cracks in

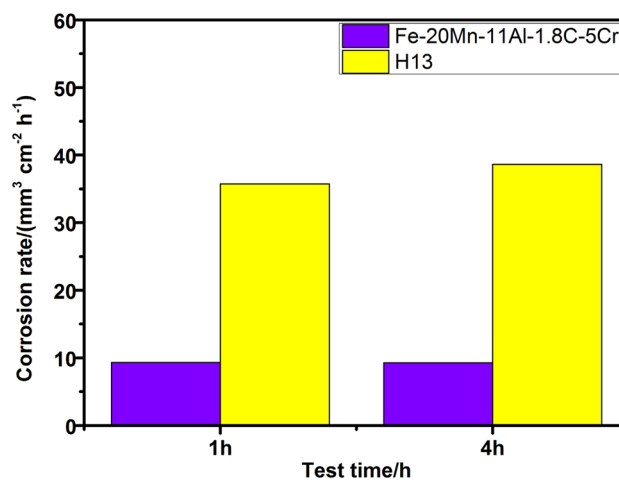


**Fig. 2** Corrosion rates of Fe-20Mn-11Al-1.8C-5Cr and H13 steel

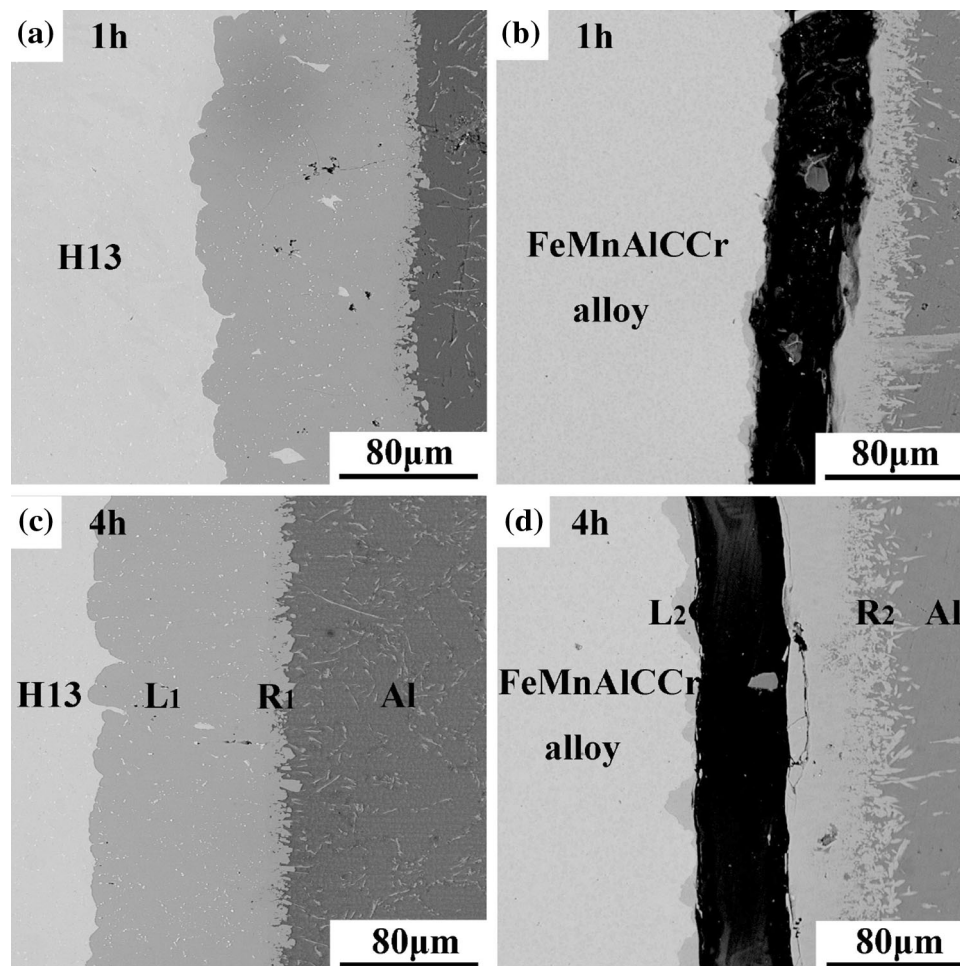


**Fig. 3** Cross-sectional images of corrosion interface after being immersed in 750 °C Al melt

this intermetallics layer propagate parallel to the specimen surface. Some solidified Al is observed in layer R immediately close to the outer Al layer, indicating the inward diffusion of Al into the substrate due to the porous structure of R<sub>1</sub> and R<sub>2</sub>. The cross-sectional images of the corrosion interface between layer R and the outer Al layer are different for H13 steel and Fe–20Mn–11Al–1.8C–5Cr alloy. As for H13 steel, the interface R<sub>1</sub> grows into the solidified Al with serrate-like shape as shown in Fig. 3c. However, the interface R<sub>2</sub> for Fe–20Mn–11Al–1.8C–5Cr alloy is relatively porous and presents some irregular products toward the outer Al layer as shown in Fig. 3d. Additionally, Fig. 3 shows that white short rod-shaped phases are present in the outer Al layer for two materials, suggesting dissolution of the substrate alloying elements into the Al melt and forming Al-rich compound, or detachment of intermetallics into the Al melt. It is interesting that the amount of white short rod-shaped phases distributed in the solidified Al layer for H13 steels is more than that for Fe–20Mn–11Al–1.8C–5Cr alloys, indicating that the dissolution of substrate alloying elements or detachment of

intermetallics into the Al melt in the case of H13 steel may be faster than that of Fe–20Mn–11Al–1.8C–5Cr alloy. In addition, the thickness of the intermetallic layer for Fe–20Mn–11Al–1.8C–5Cr alloy is thinner than that for H13 steel at the same immersion time irrespective of the thickness of crack, which will be explained hereinafter. Evidently, the intermetallic layer for Fe–20Mn–11Al–1.8C–5Cr alloy at 4 h (Fig. 3d) is thicker than that at 1 h (Fig. 3b); however, the intermetallic layer for H13 steel at 4 h (Fig. 3c) is thinner than that at 1 h (Fig. 3a). These variation trends are similar to previous studies [20, 22].

### 3.3 Corrosion products

Figure 4 shows the mapping results of the interface of Fe–20Mn–11Al–1.8C–5Cr alloy after immersion testing at 750 °C for 4 h by using EPMA. It can be seen that Al, Fe, Mn and Cr are present in the intermetallic layer, and contents of Al and Fe between the two layers are different. The concentration of Al in layer R<sub>2</sub> is higher than that in layer L<sub>2</sub>, and the concentration of Fe in layer R<sub>2</sub> is lower

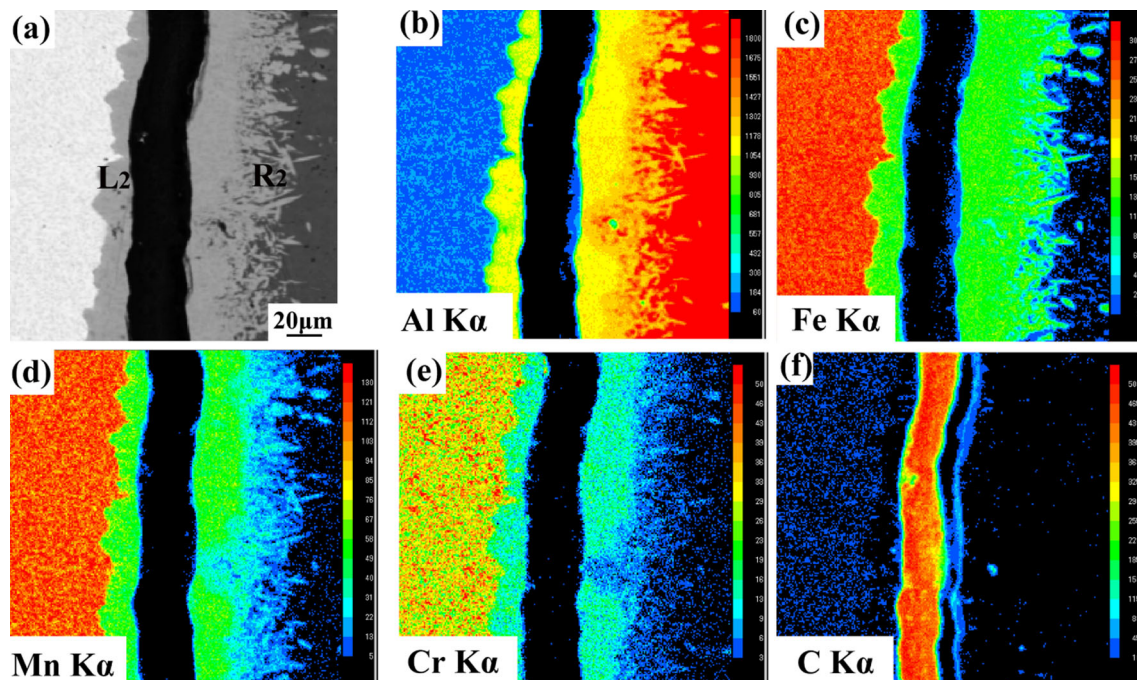


**Fig. 4** EPMA image of interfacial morphology (a) and corresponding element distribution (b–f) of Fe-20Mn-11Al-1.8C-5Cr alloy after immersion testing at 750 °C for 4 h

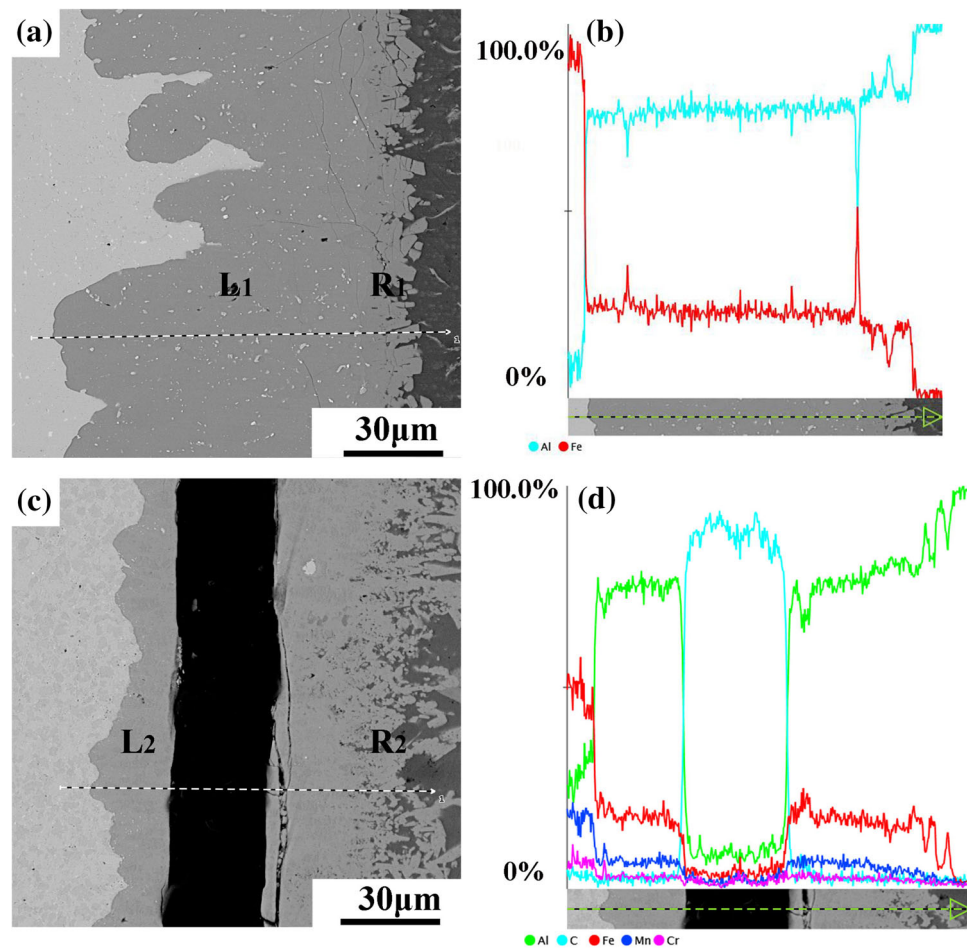
than that in layer  $L_2$ . Inward diffusion of Al into relatively porous layer  $R_2$  could be one reason for this. Meanwhile, it is also possibly due to the presence of different intermetallic compounds containing different contents of Al and Fe at the interface between molten aluminum and Fe-20Mn-11Al-1.8C-5Cr alloy.

Figure 5 shows the back scattered electron (BSE) images of corrosion interface and corresponding line-scan profiles of phases in H13 steel and Fe-20Mn-11Al-1.8C-5Cr alloy after being immersed in 750 °C molten aluminum for 4 h. As can be seen from Fig. 5b, content of Al went up when the scanning line approaches layer  $R_1$ , while content of Fe declined, suggesting that layer  $L_1$  contains more Fe and layer  $R_1$  near the outer Al layer contains more Al. In the case of Fe-20Mn-11Al-1.8C-5Cr alloy, the concentration variations of Fe, Mn, Al, C and Cr along the scanning line identified in Fig. 5c are shown in Fig. 5d. It can be seen that the concentration of Al, Fe, Mn and Cr between layer  $L_2$  and  $R_2$  exhibits obvious differences. The intermetallic layer  $L_2$  near substrate contains more Fe and the intermetallic layer  $R_2$  near the solidified Al contains more Al.

Figure 6a, b shows magnified micrographs of the layers  $L_1$  and  $R_1$  of H13 as shown in Fig. 5a. The intermetallic compound formed in the interface between the layer  $L_1$  and H13 steel substrate is typically tongue-like, which is consistent with structure as shown in Fig. 3c. Meanwhile, some small cracks at the interface between layer  $L_1$  and  $R_1$  could be observed as shown in Fig. 6b, which means that

the bonding between different layers  $L_1$  and  $R_1$  is weak. Although these cracks are small, they are quite irregular and propagate into layer  $L_1$  and layer  $R_1$ . Gradual propagation of these cracks would result in detachment of intermetallics into Al melt, which could account for the decrease of intermetallics thickness for H13 steel as shown in Fig. 3a, c. For H13 steel, the corrosion products after being immersed in molten aluminum have been generally accepted to be  $Fe_4Al_{13}$  and  $Fe_2Al_5$  [20, 22, 24]. Figure 6c, d shows magnified micrographs of the layers  $L_2$  and  $R_2$  of Fe-20Mn-11Al-1.8C-5Cr as shown in Fig. 5c. The magnified micrograph shows that the layer  $L_2$  is dense and there are at least two different regions (regions 1 and 2) in the layer  $L_2$  (Fig. 6c), while layer  $R_2$  is more porous especially at the position immediately adjacent to the solidified Al (Fig. 6d). The presence of two different regions in layer  $L_2$  is related to the microstructure of Fe-20Mn-11Al-1.8C-5Cr substrate consisting of two main constituent phases ( $\gamma$  and  $(Fe, Mn)_3AlC_x$ ) with different contents of Mn and Cr as shown in Fig. 1. According to the EDS results of regions 1–4 in Fig. 6c, d as listed in Table 2, the two phases formed in layer  $L_2$  and  $R_2$  are probably  $(Fe, Mn, Cr)_2Al_5$  and  $(Fe, Mn, Cr)_4Al_{13}$ , respectively. Moreover, thickness of layer  $L_2$  is bigger than that of layer  $R_2$  as shown in Fig. 5c, suggesting that the volume of intermetallics in layer  $L_2$  is bigger than that in layer  $R_2$ .

Figure 7 shows the XRD pattern of the corrosion products formed on the present Fe-20Mn-11Al-1.8C-5Cr alloy after immersing in 750 °C Al melt for 4 h after



**Fig. 5** BSE image of phase microstructure at corrosion interface after being immersed in 750 °C molten aluminum for 4 h (**a**, **c**), and corresponding element distribution by line scan (**b**, **d**). **a**, **b** H13 steel; **c**, **d** Fe–20Mn–11Al–1.8C–5Cr alloy

removing the solidified Al from the specimen. Diffraction peaks very close to  $\text{Fe}_2\text{Al}_5$  and  $\text{Fe}_4\text{Al}_{13}$  intermetallics were observed. Since the BSE micrographs (Fig. 3) as well as EDS and EPMA analysis (Figs. 4, 5 and 6) show that there are two phases with different contents of Fe, Mn, Al and Cr in the intermetallic layers, the two corrosion products in layer L<sub>2</sub> and R<sub>2</sub> (as shown in Fig. 6c, d) could be confirmed to be  $(\text{Fe}, \text{Mn}, \text{Cr})_2\text{Al}_5$  and  $(\text{Fe}, \text{Mn}, \text{Cr})_4\text{Al}_{13}$ , whose crystal structures are similar to that of  $\text{Fe}_2\text{Al}_5$  and  $\text{Fe}_4\text{Al}_{14}$ , respectively. This product is different from that examined by Su et al. [26] in the hot-dip aluminizing of Fe–8Al–30Mn–0.8C alloy, in which they reported that only  $(\text{Fe}, \text{Mn})_2\text{Al}_5$  intermetallics formed on the substrate. The difference of the lattice parameters between  $(\text{Fe}, \text{Mn}, \text{Cr})_2\text{Al}_5$  and  $\text{Fe}_2\text{Al}_5$ , as well as the difference of the lattice parameters between  $(\text{Fe}, \text{Mn}, \text{Cr})_4\text{Al}_{13}$  and  $\text{Fe}_4\text{Al}_{13}$ , which is attributed to the different atomic radii of Fe, Mn and Cr atoms, may account for the minor difference between diffraction peaks positions of  $(\text{Fe}, \text{Mn}, \text{Cr})_2\text{Al}_5$  and  $\text{Fe}_2\text{Al}_5$ , as well as the minor difference between diffraction peaks positions of  $(\text{Fe}, \text{Mn}, \text{Cr})_4\text{Al}_{13}$  and  $\text{Fe}_4\text{Al}_{13}$ . In addition,

diffraction peaks of  $(\text{Fe}, \text{Mn})_3\text{AlC}_x$  and  $\text{Cr}_7\text{C}_3$  could also be observed, while no diffraction peak of  $\gamma$  could be observed, which indicated that some  $(\text{Fe}, \text{Mn})_3\text{AlC}_x$  and  $\text{Cr}_7\text{C}_3$  carbides exist within the corrosion products. This indicates that there is incomplete even no reaction between  $(\text{Fe}, \text{Mn})_3\text{AlC}_x$  and molten aluminum as well as between  $\text{Cr}_7\text{C}_3$  and molten aluminum when being immersed in molten aluminum. That is to say, the corrosion resistance of  $(\text{Fe}, \text{Mn})_3\text{AlC}_x$  and  $\text{Cr}_7\text{C}_3$  carbide in Al melt is better than that of  $\gamma$  matrix.

## 4 Discussion

At first, there are two ways to understand why the corrosion rate of Fe–20Mn–11Al–1.8C–5Cr alloy is smaller than that of H13. On the one hand, the presence of  $\kappa$ -carbide plays a key role in enhancing the corrosion resistance of Fe–20Mn–11Al–1.8C–5Cr alloy in molten aluminum. Zhang et al. [27] indicated that  $\kappa$ -carbide could exist between steel substrate and diffusion layers after hot-dip aluminizing,

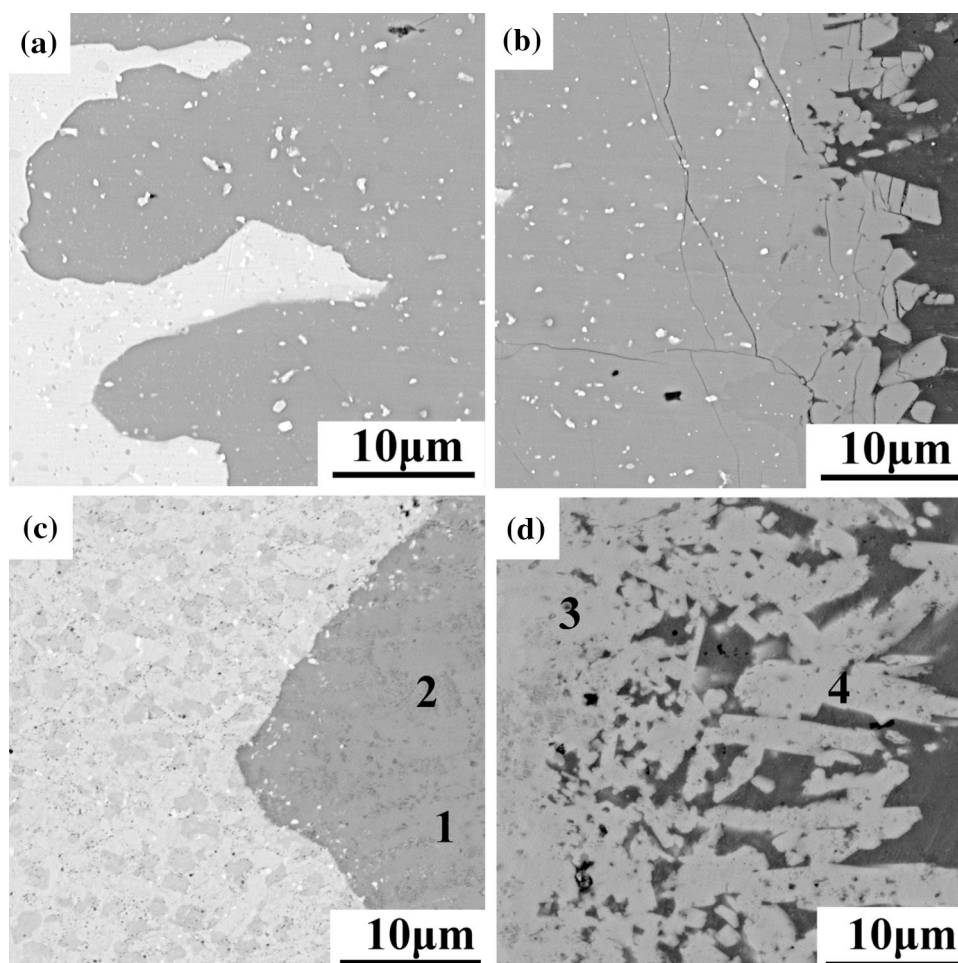


**Fig. 6** Magnified BSE micrographs of reaction interface layers formed on specimens after immersing in 750 °C Al melt for 4 h: layers  $L_1$  (a) and  $R_1$  in Fig. 5a, and layers  $L_2$  (c) and  $R_2$  (d) in Fig. 5c

**Table 2** Chemical composition of phases analyzed by EDS/SEM (at.%)

Position	Al	Fe	Mn	Cr	C	Phases composition
1	71.73	16.20	6.47	1.64	3.95	$(\text{Fe, Mn, Cr})_2\text{Al}_5$
2	70.19	18.20	5.61	1.48	4.53	$(\text{Fe, Mn, Cr})_2\text{Al}_5$
3	74.31	16.93	4.02	1.36	3.38	$(\text{Fe, Mn, Cr})_4\text{Al}_{13}$
4	80.26	12.35	3.68	1.32	2.39	$(\text{Fe, Mn, Cr})_4\text{Al}_{13}$

indicating that the  $\kappa$ -carbide has good durability in Al melt. XRD result in Fig. 7 confirms the presence of  $\kappa$ -carbide in the corrosion products. On the other hand, Xu et al. [25] pointed that durability of alloys in metal melt depends on their lattice structure to a large extent, and the durability of FCC structured alloy is better than that of BCC structured alloy possibly due to the compactness of the atomic structure. FCC structured  $\gamma$  matrix of Fe–20Mn–11Al–

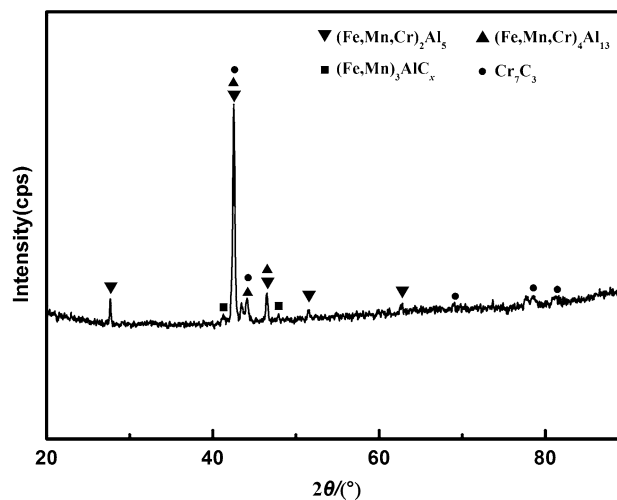


**Fig. 7** X-ray diffraction pattern of corrosion products formed on the present Fe–20Mn–11Al–1.8C–5Cr alloy after immersing in 750 °C Al melt for 4 h

1.8C–5Cr alloy has atomic structure more dense than that of the BCC Fe in H13. Therefore, it is reasonable to believe that the durability of  $\gamma$  matrix is better than that of BCC Fe in H13. In addition,  $\text{Al}_2\text{O}_3$  and  $\text{Cr}_7\text{C}_3$  carbide are inert in molten aluminum [1], which can also prevent the direct contacting of Fe and Al melt. This will decrease the growth of intermetallics, which can explain why the thickness of the intermetallic layer for Fe–20Mn–11Al–1.8C–5Cr alloy is thinner than that for H13 steel at the same immersing time irrespective of the thickness of crack.

Second, it is generally considered that the compositions of alloy and Al melt significantly affect the microstructure and morphology of corrosion products [28]. Several studies [25, 29] pointed that tongue-like interface between the  $\text{Fe}_2\text{Al}_5$  and H13 is often formed due to the peculiar *c*-axis of  $\text{Fe}_2\text{Al}_5$ . In the case of alloy steel, on the one hand, Chen and Wang [30] and Akdeniz and Mekhrabov [31] pointed that Cr can reduce the growth rate of the intermetallic layer and make the steel/intermetallic interfaces more smoother. Therefore, it can be concluded that Cr can take up the vacant sites in the *c*-axis of  $\text{Fe}_2\text{Al}_5$  and decrease the diffusion rate of Al atoms in  $\text{Fe}_2\text{Al}_5$ , resulting in a more flatter substrate/ $(\text{Fe}, \text{Cr})_2\text{Al}_5$  interface. On the other hand, Su et al. [26] pointed that Mn can enhance the growth rate of  $\text{Fe}_2\text{Al}_5$  intermetallic and result in a tongue-like interface. It can be seen that the tongue-like structure in the present Fe–20Mn–11Al–1.8C–5Cr alloy is similar to that in Fe–8Al–30Mn–0.8C alloy, which indicates that the effect of Mn on the growth rate of  $(\text{Fe}, \text{Mn}, \text{Cr})_2\text{Al}_5$  is more remarkable than that of Cr in this work.

Finally, the formation mechanism of cracks at the interface is complex. In the case of H13 steel, the cracks form at the interface between  $\text{Fe}_2\text{Al}_5$  intermetallic layer and  $\text{F}_4\text{Al}_{13}$  intermetallic layer and propagate into two intermetallics layers. The stresses produced during the growth of the formed intermetallics and the cooling process, which resulted from different coefficients of thermal expansion between different intermetallic layers and Al, may account for these cracks [22, 31]. Hence, cracks formed in Fe–20Mn–11Al–1.8C–5Cr alloys are mainly due to the tensile stress resulted from different thermal expansion coefficients of the intermetallic layer in comparison with the Fe–20Mn–11Al–1.8C–5Cr alloy matrix. In addition, mechanical polishing could also result in cracks due to the brittleness of intermetallics.

## 5 Conclusion

The corrosion behavior of a spark plasma sintering processed Fe–20Mn–11Al–1.8C–5Cr alloy in a 750 °C molten aluminum was investigated by immersing test. The corrosion rate of the as-sintered Fe–20Mn–11Al–1.8C–5Cr alloy

in molten aluminum is lower than that of H13, which is mainly due to the presence of  $\kappa$ -carbide  $((\text{Fe}, \text{Mn})_3\text{AlC}_x)$ ,  $\text{Cr}_7\text{C}_3$  carbide and  $\text{Al}_2\text{O}_3$  in the alloy. Their corrosion rates in Al melt are lower than those of the  $\gamma$  phase and BCC Fe. Furthermore,  $((\text{Fe}, \text{Mn})_3\text{AlC}_x)$  and  $\text{Cr}_7\text{C}_3$  carbide can take on the role of root to grasp the corrosion product and restrain them from spalling. The intermetallic layers formed on the surface of the as-sintered Fe–20Mn–11Al–1.8C–5Cr alloy after immersing test consisted of a majority of  $(\text{Fe}, \text{Mn}, \text{Cr})_2\text{Al}_5$  layer, and a minority of  $(\text{Fe}, \text{Mn}, \text{Cr})_4\text{Al}_{13}$  layer. These Mn–Cr-containing corrosion products can also act as an effective diffusion barrier to retard the interfacial reactions between Fe–20Mn–11Al–1.8C–5Cr alloy and molten aluminum. Certainly, the FCC structure in Fe–20Mn–11Al–1.8C–5Cr matrix is also beneficial to the better corrosion resistance of Fe–20Mn–11Al–1.8C–5Cr alloy than that of H13 steel.

**Acknowledgements** This research was funded by National Natural Science Foundation of China (51271080) and Opening Project of Guangdong Key Laboratory for Advanced Metallic Materials Processing (South China University of Technology) (Grant No. GJ201609).

## References

- [1] M. Yan, Z. Fan, *J. Mater. Sci.* 36 (2001) 285–295.
- [2] W. Cheng, C. Wang, *Appl. Surf. Sci.* 257 (2011) 4663–4668.
- [3] K. Bouché, F. Barbier, A. Coulet, *Mater. Sci. Eng. A* 249 (1998) 167–175.
- [4] A. Bouayad, C. Gerometta, A. Belkebir, A. Ambari, *Mater. Sci. Eng. A* 363 (2003) 53–61.
- [5] D. Balloy, J.C. Tissier, M.L. Giorgi, M. Briant, *Metall. Mater. Trans. A* 41 (2010) 2366–2376.
- [6] X.M. Zhang, H.F. Luo, L.Y. Shi, *J. Iron Steel Res. Int.* 23 (2016) 1127–1133.
- [7] D.G. Morris, M.A. Muñoz-Morris, L.M. Requejo, *Acta Mater.* 54 (2006) 2335–2341.
- [8] G.D. Tsay, C.L. Lin, C.G. Chao, T.F. Liu, *Mater. Trans.* 51 (2010) 2318–2321.
- [9] Y.H. Tuan, C.S. Wang, C.Y. Tsai, C.G. Chao, T.F. Liu, *Mater. Chem. Phys.* 114 (2009) 595–598.
- [10] D. Song, W. Sun, J.Y. Jiang, H. Ma, J.C. Zhang, Z.J. Cheng, *J. Iron Steel Res. Int.* 23 (2016) 608–617.
- [11] J.G. Duh, C.J. Wang, *J. Mater. Sci.* 25 (1990) 268–276.
- [12] X.Y. Chong, Y.H. Jiang, R. Zhou, *J. Am. Ceram. Soc.* 100 (2017) 1588–1597.
- [13] J. Liu, W. Chen, Z. Jiang, L. Liu, Z. Fu, *Vacuum* 137 (2017) 183–190.
- [14] K.G. Chin, H.J. Lee, J.H. Kwak, J.Y. Kang, B.J. Lee, *J. Alloy. Compd.* 505 (2010) 217–223.
- [15] M.C. Li, H. Chang, P.W. Kao, D. Gan, *Mater. Chem. Phys.* 59 (1999) 96–99.
- [16] C. Suryanarayana, *Prog. Mater. Sci.* 46 (2001) 1–184.
- [17] Z.A. Munir, U. Anselmi-Tamburini, M. Ohyanagi, *J. Mater. Sci.* 41 (2006) 763–777.
- [18] V. Mamedov, *Powder Metall.* 45 (2002) 322–328.
- [19] R. Vintila, A. Charest, R.A.L. Drew, M. Brochu, *Mater. Sci. Eng. A* 528 (2011) 4395–4407.



- [20] X.M. Zhang, W.P. Chen, H.F. Luo, S. Li, T. Zhou, L.Y. Shi, *Corros. Sci.* 125 (2017) 20–28.
- [21] D.C. Lou, O.M. Akselsen, M.I. Onsjøien, J.K. Solberg, J. Berget, *Surf. Coat. Technol.* 200 (2006) 5282–5288.
- [22] X.M. Zhang, Research on the corrosion-wear resistance of the novel Fe–Cr–B cast steels and their three-dimensional interconnected ZrO<sub>2</sub> reinforced metal matrix composites in molten aluminum, South China University of Technology, Guangzhou, 2015.
- [23] D. Wang, Z. Shi, L. Zou, *Appl. Surf. Sci.* 214 (2003) 304–311.
- [24] H.Q. Xiao, W.P. Chen, Z. Liu, *Trans. Nonferrous Met. Soc. China* 22 (2012) 2320–2326.
- [25] J. Xu, M.A. Bright, X. Liu, E. Barbero, *Metall. Mater. Trans. A* 38 (2007) 2727–2736.
- [26] C.W. Su, J.W. Lee, C.S. Wang, C.G. Chao, T.F. Liu, *Surf. Coat. Technol.* 202 (2008) 1847–1852.
- [27] W. Zhang, J.B. Wen, X.F. Wang, F. Xiong, X.A. Cui, *Trans. Nonferrous Met. Soc. China* 17 (2007) 1632–1636.
- [28] M.V. Akdeniz, A.O. Mekhrabov, T. Yilmaz, *Scripta Mater.* 31 (1994) 1723–1728.
- [29] S.G. Denner, R.D. Jones, *Mater. Sci. Technol.* 4 (1977) 167–174.
- [30] W.J. Cheng, C.J. Wang, *Appl. Surf. Sci.* 277 (2013) 139–145.
- [31] M.V. Akdeniz, A.O. Mekhrabov, *Acta Mater.* 46 (1998) 1185–1192.